Microalgae bio-reactive façade: a radiative-convective model powered by hourly illumination computation and historical weather data
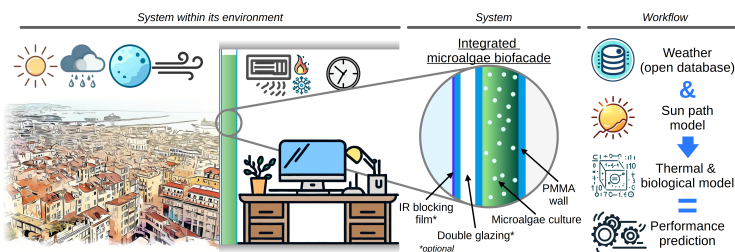
Victor Pozzobon[1] ✉

[1]LGPM, CentraleSupélec, Université Paris-Saclay, SFR Condorcet FR CNRS 3417, Centre Européen de Biotechnologie et de Bioéconomie (CEBB), 3 rue des Rouges Terres 51110 Pomacle, France

This article presents a numerical model predicting the performance of a microalgae biofaçade. The core of the model is the association of radiative, convective, and conductive heat transfers. These key physical phenomena are modulated by actual weather data and coupled to a biological model of the microalga *Chlorella vulgaris*. Based on the conjunction of temperature and illumination predictions, the biofaçade performances are categorized between low, adequate, high temperature × light-deficient, light-sufficient conditions. The capabilities of the model (dissection of acute events to year-round performance prediction) are illustrated using the city of Marseille, France, over the year 2020. The numerical behavior of the model itself is then analyzed. The influence of the Urban Heat Island submodel is discussed, and a global sensitivity analysis (Sobol's indices) is led to assess the impact of uncertain physical parameters. The model accuracy is evaluated at 7.4 % of the total daytime (under conservative assumptions) . The most influential parameters are the microalgae culture emissivity and the building indoor emissivity. All in all, the confidence in this model is high enough so that it can be used to design a biofaçade numerically.

Graphical abstract

Microalgae | Biofaçade | Modeling | Hourly illumination | Weather data
Correspondence: *victor.pozzobon@centralesupelec.fr*

1. Introduction

Façade-integrated microalgae photobioreactors (in short bioreactive façades or biofaçades) are regarded as a potential synergy between a building and a biological system, belonging to a group of technological solutions paving the way toward high-performance architectures (1, 2). Indeed, combining the microalgal and advanced building technologies could bring benefits greater than the sum of each one taken individually. On the microalgae side, production technologies are often divided into two categories: open systems (such as raceway ponds) and closed systems (or photobioreactors). The first ones are inexpensive but have low productivity and high land requirement. Their modest performances can be explained by their ease of contamination and large volume, making them difficult to control (*e.g.*, modifying the culture medium temperature). On the contrary, closed systems are more compact, often well-instrumented, and highly controlled. Consequently, they are more costly. Therefore, integrating them in a building could help reduce their costs by providing vertical support, utilities (water, thermal regulation, ...), and possibly nutrients (carbon dioxide recovered from the building, for example). On the building side, benefits are also anticipated. Integrating photobioreactors could provide shading, improve thermal comfort (by modulating incident heat better than glazing in summer), generate revenues, and be considered aesthetic enhancements.

Despite the great promises of this technology, to date, only a few studies can be found in the literature. Among them, the experimental investigation of Pruvost *et al.* is of note (3). The authors investigated *Chlorella vulgaris* growth in this type of culture device in the context of CO_2 biofixation. The test campaign lasted one year and delivered key figures to assess the device's biotechnological performance. In addition, the authors showed that the energetic relevance of such a system was conditioned to optimal thermal interaction with the building hosting it. Nevertheless, they also acknowledge that fine understanding and modeling of thermal integration was complex and laid outside of the scope of their work.

Thermal performances of a biofaçade are not only crucial from a biotechnological point of view, but they are also pivotal from a building efficiency perspective. Indeed, most of the thermal losses occur through the façade (4). It is therefore important to qualify and limit the system's overall thermal conductivity, or U value. Surprisingly, as pointed out by Umdu *et al.*, only scarce literature deals with this aspect of biofaçade. In an effort to fill this gap, Umdu's team led a systematic investigation of the geometrical parameters influencing the system's thermal behavior (reservoir depth, structural layer material and depth, air layer addition, and depth) (4). The authors concluded that PMMA should be preferred over glass as a glazing material to reduce building static load. Fur-

thermore, the addition of an air layer dramatically cut the U value of the whole system (from 53 to 3 W/m^2/K in the most favorable case).

In addition to sole technical considerations, Sarmadi *et al.* investigated numerically the question of the visual comfort associated with microalgae biofaçade (5). The case study was a modern office building which a mezzanine located in Tehran. Visual comfort is a trade-off between sunlight availability and potentially blinding glare. The authors concluded that microalgae biofaçades efficiently reduce blinding glare occurrence and intensity in such a sunny environment. Yet, they had to be blended with conventional double-glazing to prevent too-dark configurations from emerging. Going further in refining the technology's aesthetic, it is also possible to divide the biofaçade into several culture compartments, each hosting microalgal species of different color (6).

Finally, perhaps the most important study to be reported is the deployments of 185 m^2 of biofaçade in the BIQ house in Hamburg (7) (Fig. 1 - Left). This field trial helped the technology make a significant leap forward. The biofaçades were installed as a second skin to the building. The modules were made of glass, 2.5-meter-high, with an 18 mm cultivation compartment and an air layer (branded as *SolarLeaf*). Over the course of the year 2014, the system achieved 4.4 % solar-to-biomass conversion efficiency, with compares well with laboratory studies on microalgae photoconversion efficiency (*e.g.*, 5.01 % (8), 5.65 % (9), or 4.34 % (10)) and 21 % thermal energy recovery efficiency. Furthermore, the tests again highlighted the pivotal role of temperature on *Chlorella vulgaris* growth. Taking a step back from technical considerations, this field deployment also demonstrated especially good social acceptance of the technology.

In all the studies above, scholars emphasized the pivotal role of the thermal management of the system. Indeed, microalgae are cells of a few micrometers, incapable of regulating their temperature. Their inability to manipulate their temperature is all the more detrimental as this parameter is key to their bloom or collapse. Indeed, it controls, among others, enzymes' reaction rates and affinities. High temperatures (above 45 °C for mesophilic species, 55-60 °C for extremely tolerant microalgae) can even denature protein and DNA irreversibly (11). On the contrary, freezing temperatures can induce the growth of large ice crystals within the cells lethally damaging them (12). Yet, knowing the thermal behavior of a biofaçade is complex as it results from:

- Direct incident illumination from the sun, which provides both the photosynthetically active radiation required for the microalgae to grow and heat (infrared part of the spectrum),

- Radiative heat exchange with the sky, which also provides photosynthetically active and thermal radiation but can also cool the system down, especially at night,

- Radiative heat exchange with the surrounding (buildings, fields, ... depending on the location),

- Convective heat exchange with the outdoor air,

- Radiative and convective exchange with the building hosting the biofaçade,

- Heat supplied and removed by the gas flow sparging within the culture medium.

In addition to the diversity of the heat exchange phenomena at stake, another aspect amplifies the complexity of the prediction of a microalgae biofaçade temperature: the thermal dynamics of the system's environment. Indeed to properly assess the performances of a biofaçade system, all these phenomena are to be accounted with hour-scale dynamics over at least one year, as they are modulated by the day/night and year-round cycles, as well as the weather (wind velocity, cloud cover, air temperature, ...). Coupling all those aspects in a time-resolute model before assessing microalgae growth is the goal of this work.

Therefore, the major challenge lies in gathering and coupling models for each of the phenomena at stake. Luckily, for most of them, scholars provide mature models (*e.g.*, direct sunlight with for cloud cover (13), sky temperature (14), urban heat island phenomenon (15), ...) and the public French weather forecast agency (Météo-France) released a large amount of data allowing to simulate actual weather conditions. Finally, to yield relevant assessment, the thermal behavior of the system and illumination have to be matched with microalgal cells requirement. *Chlorella vulgaris* was chosen as the model strain as it is commonly encountered in both industrial and scientific communities, is approved as food and feed by (EFSA - Ares (2022) 1668627 - and US FDA - GRN 00396 -), and features a sizable biotechnological potential (16). Here again, recent studies have provided insight into cell growth under varying light (17, 18) and temperature (19), which allow modeling its performances.

With all these tools at hand, it seems reasonable to believe that one can produce a model that faithfully predicts microalgae biofaçade operational environment. The purpose of this model is clear: screen microalgae biofaçade designs systematically to identify the optimal geometrical configuration and operating procedure for any foreseen building implementation (location, orientation, weather conditions). Therefore, it would pave the way to location-specific best-achievable performance prediction, aiming at advising on the economic and environmental relevance of a microalgae biofaçade deployment.

This article is the first of a set of two. It presents the development of the model, with all the details necessary for its reproduction. First, the system is introduced, and the phenomena at stake are listed. Then, assumptions and submodels are introduced before being coupled. Consequently, the convergence of the numerical parameters (timestep, initial transient duration, ...) is checked, and construction hypotheses are validated. Once constructed, the model will be applied to an illustrative case: the city Marseille (South of France on the Mediterranean coast) over the year 2020. This location was chosen for its high number of sunny days, hence its high potential for photosynthetic microorganisms cultivation. The performances will be simulated over the year 2020 to avoid
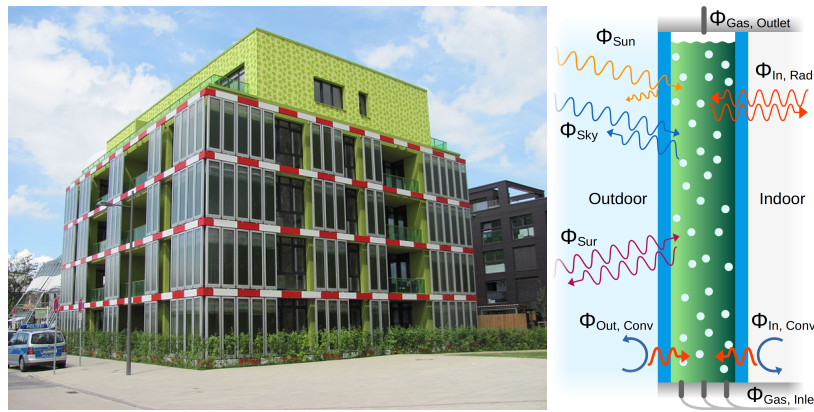
Fig. 1. On the left, the BIQ house, Hamburg, Germany, with microalgae biofaçade implemented as double skin. On the right, the schematic representation of the considered microalgae biofaçade, implemented as glazing. The reported heat fluxes (Φ) are introduced in the text

artifacts linked to an exceptionally cold or hot year (like 2021 and 2022). The model capabilities are illustrated over three timescales: hour, week, and year. Once showcased, the numerical behavior of the model is further analyzed: the influence of the submodels for which confidence is low is investigated, and a global sensitivity analysis (Sobol's indices) is led to assess the impact of uncertain parameters. Finally, the influence of the biofaçade design on the numerical behavior of the model is screened by testing single vs. double-glazing configurations.

2. Considered system

Figure 1 (Right) presents a schematic representation of the considered microalgae biofaçade. The system is made of a reservoir hosting the microalgae culture (5 cm depth, e_{mc}, as advised by several authors (1, 4, 20)). This reservoir is surrounded by 1.5 cm thick PMMA sheets. The PMMA is preferred over the glass as it is much lighter (1200 kg/m^3 vs. 2500 kg/m^3) to reduce the static load on the building façade. The double glazing compartment hosts 1.5 cm of stagnant air thanks to another 1.5 cm PMMA glazing (20). Therefore, the system's dimensions are 11.5 cm in depth, 1 m in width (w_{mc}), and 4 m in height (H_{mc}, standard floor height in office buildings).

The considered heat fluxes are:

- incident direct sunlight, Φ_{Sun} which will be divided into visible and infrared radiation,

- incident and emitted radiation towards the sky, Φ_{Sky},

- incident and emitted radiation towards the surroundings, Φ_{Sur},

- incident and emitted radiation towards the host building indoor, $\Phi_{In,Rad}$,

- convective-conductive exchange with the outdoor air, $\Phi_{Out,Conv}$,

- convective-conductive exchange with the indoor air, $\Phi_{In,Conv}$,

- heat inflow from the sparged gas, $\Phi_{Gas,Inlet}$, and heat outflow from the vented gas, $\Phi_{Gas,Outlet}$.

All those fluxes will contribute to the thermal balance of the system. Yet, several other pieces of information are needed to model the biofaçade properly. First, the microalgae culture is assumed to be relatively healthy. Its concentration is adjusted to let through a desired fraction (α, typically 50 %) of the green radiation. This wavelength selection is made possible because microalgae adsorb twice more efficiently red and blue light than green light (21). Therefore, it would exhibit an excepted intense green color. On top of aesthetic consideration, this implies a refinement of how visible radiation is treated. Part of its energy will be directed toward photosynthesis, while the other will be converted to heat. Second, the system is integrated into an office building façade at a height somewhat higher than the surrounding building (E_{mc} = 20 m), to ensure adequate sunlight access, and placed in the middle of the façade, to ease the consideration about outdoor convective heat transfer induced by the wind. Finally, the building occupant's comfort lies out of the scope of this work. However, visual transmission and indoor humidity can be impacted by the microalgae biofaçade. The first one could be adjusted by alternating biofaçade and conventional glazing. The second could also be manipulated by choosing at the design stage if the system vent is oriented towards the outdoor or the indoor.

3. Heat flux models

3 1. Incident direct solar radiation

Incident direct solar radiation (Φ_{Sun}) comprises ultraviolet, visible, and infrared radiation. Visible radiation will be separated from the two others as it represents the fraction capable of triggering photosynthesis (Eq. 1). Another reason is that the model proposed by the Illuminating Engineering Society - used in this work - yields sunlight predictions in klux, hence accounting for the visible part of the spectrum. This model is quite complex. In a nutshell, it computes both solar and sky illumination ($\Phi_{Sun,Vis}$ and $\Phi_{Sky,Vis}$, respectively) based on solar time, position on Earth, cloud cover, and orientation. For more details, the interested reader is kindly re-

ferred to the original article ([13]). Nevertheless, knowing that the visible part of the solar spectrum represents 48.7 % of its energy ([22]), and that 1 solar klux represents 7.9 W/m^2, it is possible to derive $\Phi_{Sun,IR}$ (Eq. [2]).

$$\Phi_{Sun} = \Phi_{Sun,Vis} + \Phi_{Sun,IR} \qquad (1)$$

$$\Phi_{Sun,IR} = (\frac{1}{0.487} - 1)\Phi_{Sun,Vis} = 1.05\Phi_{Sun,Vis} \qquad (2)$$

Before reaching the culture, the incident solar fluxes have to cross several interfaces (depending on the number of glazing, n_{Glaz}). At each interface, reflectivity has to be accounted for. The classical equation for non-polarized light at a perfect dielectric interface was used (Eq. [3]) ([23]):

$$R_{interface} = \frac{1}{2}\left[\frac{\tan^2(\theta_i - \theta_r)}{\tan^2(\theta_i + \theta_r)} + \frac{\sin^2(\theta_i - \theta_r)}{\sin^2(\theta_i + \theta_r)}\right] \qquad (3)$$

Where the incidence angle (θ_i) is given by the sun path model and the reflection angle (θ_r) by Snell's law. One should note that, as the system features several interfaces the evolution of the incidence from one interface to the other has to be accounted for. Hence, the overall transmission (τ_{Sun}) is the product of the transmission at each interface. For the sake of simplicity, in these computations, multiple internal reflections were neglected.

Finally, the question of radiation absorption is to be addressed. The infrared component can be assumed entirely absorbed, as 5 cm of water represents a barrier stopping all radiation above 900 nm ([24]). In the case of the visible energy reaching the culture, its absorption is governed by microalgae concentration and intrinsic spectral properties (lumped into the previously introduced α factor). Of this absorbed power, only a fraction will be used for photosynthesis ($\eta_{ps} = 4.34$ % for *Chlorella vulgaris* in proper conditions ([10])), the rest being turned into heat. Therefore, the absorbed fraction of the incident solar power is given by Equation [4] (where the $\frac{3-2\alpha^2-\alpha}{3}$ accounts for the different selective absorptions between blue, green,and red lights).

$$\Phi_{Sun,Abs} = \tau_{Sun}(\frac{3-2\alpha^2-\alpha}{3}(1-\eta_{ps})\Phi_{Sun,Vis} \\ + 1.05\Phi_{Sun,Vis}) \qquad (4)$$

3 2. Sky radiation

Like incident direct solar radiation, sky incident radiation comprises ultraviolet, visible, and infrared components. Still, the distribution between them is less certain than for the sun. Therefore, two models were used to describe this incident flux. Total power ($\Phi_{Sky,Tot}$) was calculated using a sky temperature model. Sky temperature is a concept that allows computing this incident heat flux using an equation similar to the Stefan-Boltzmann formula (Eq. [5]) ([25]). All the complexity is, therefore, to evaluate the $\epsilon_{Sky}T_{Sky}^4$ term. Numer-

ous types of models exist and have been reviewed recently by Evangelisti ([25]). In our case, we choose the model of Clarke ([14]) for three reasons: it is capable of reconstructing sky temperature from ambient air temperature ($T_{Air,Out}$ provided in the available weather data), it accounts for both clear and cloudy skies (via a cloud cover factor, CC, also provided in the available weather data), and its implementation has been reviewed and corrected by Ficker ([26]). Like the incident solar light model, the derivation is quite complex, and the interested reader is referred to the original handbook of Clarke. Only the final equation is reported here (Eq. [6]).

$$\Phi_{Sky,Tot} = \sigma\epsilon_{Sky}T_{Sky}^4 \qquad (5)$$

$$\begin{aligned}\epsilon_{Sky}T_{Sky}^4 =& 9.36575\ 10^{-6}(1-CC)T_{Air,Out}^6 \\ &+ T_{Air,Out}^4 CC[(1-0.84CC)(0.527 \\ &+ 0.161\exp(8.45[1-\frac{273}{T_{Air,Out}}])) \\ &+ 0.84CC]\end{aligned} \qquad (6)$$

The visible component of the sky radiation ($\Phi_{Sky,Vis}$) is obtained using Illuminating Engineering Society's model. Considerations on optics and photosynthesis efficiency are similar to ones for direct solar illumination. Thus, the question of interfaces reflectivities is to be addressed. According to Incropera ([27]), 40 % of the sky radiation can be described as originating from the sun's direction, the remaining fraction being distributed as following the cosine of the incidence angle (for 0 to 90°). Therefore, 40 % of the sky fluxes were subjected to the same reflectivity as the direct sun irradiance (τ_{Sun}, Eq. [3]). The reflectivity of the other 60 % ($\tau_{Sky,Abs}$) was computed by integrating Equation [3] over the suggested incidence angle distribution. Finally, a view factor (F_{Sky}) has to be applied to the 60 % fraction to account for the fact that the sky represents only part of the system view field. As a good rule of thumb, 0.5 is classically used ([25]), yet some refinements can be introduced depending on the surrounding (rural or urban, ...)([14]). Therefore, the absorbed sky heat flux can be written as Equation [7].

$$\begin{aligned}\Phi_{Sky,Abs} =& F_{Sky}(0.4\ \tau_{Sun} + 0.6\ \tau_{Sky,Abs}) \\ &(\frac{3-2\alpha^2-\alpha}{3}(1-\eta_{ps})\Phi_{Sky,Vis} \\ &+ (\Phi_{Sky,Tot} - \Phi_{Sky,Vis}))\end{aligned} \qquad (7)$$

The final element to account for is the thermal radiation emitted towards the sky. Only limited information is available on how to model such a term. Therefore, the classical Stefan-Boltzmann formula was chosen (Eq. [8]), with a microalgae suspension emissivity (ϵ_{mc}) taken as 0.9.

$$\Phi_{Sky,Emi} = F_{Sky}\tau_{Sky,Emi}\sigma\epsilon_{mc}T_{mc}^4 \qquad (8)$$

3 3. Surrounding radiation

In addition to exchanging heat with the sky, the microalgae biofaçade receives and emits radiation toward its surrounding. In our case, an urban environment is considered as the direct surrounding of the building hosting the biofaçade. Estimating the temperature of a city landscape is far from obvious. Indeed, its geometry is complex, the materials constituting it have diverse radiative properties, and the system has its own thermal dynamic subjected to the Urban Heat Island (UHI) phenomenon. Despite its complexity, several authors have been able to measure and model the phenomenon (recently reviewed by (15)). Among the different approaches, the UHII (for Urban Heat Island Intensity, Eq. 9) method is the most common. This method measures the Urban Heat Island magnitude as the maximum, over a day, of the difference between the city temperature (T_{Urb}, usually obtained via satellites) and the temperature of rural area in its vicinity (T_{Rur}).

$$UHII = \max(T_{Urb} - T_{Rur}) \tag{9}$$

As for any meteorological model, it is advised to choose one calibrated with data originating from a similar bioclimatic environment. Therefore, a UHII model based on data obtained in Hamburg, Germany (28), was used in this work (Eq. 10). This model is based on ground measurements of six meteorological stations. This large variety of measurement locations allowed to determine which was most representative of the city center. Furthermore, in order to improve robustness, the measurements of two stations located in the city outskirts were averaged to compute the rural area temperature. The use of ground stations (versus satellites) allowed to achieve reliable measurements, even on cloudy days, making this model especially valuable compared to studies based on satellites measurements, which are restricted to clear sky configurations (29). Finally, the data span over an extensive period of time, from 1985 to 1999, which is a token of the model quality.

$$UHII = -0.54\,\overline{U} - 1.48\,\overline{CC} - 0.039\,\overline{Y} + 7.63 \tag{10}$$

Where $\overline{U}$ is the wind velocity (in m/s), $\overline{CC}$ is cloud cover factors (between 0 and 1), and $\overline{Y}$ is the relative humidity (in %), all averaged over the day associated with the UHII value. Still, by definition, UHII provides only one value for a given day and no information on the temporal dynamics of the city center overheating compared to its rural counterpart. Studies reporting the hourly dynamic of Urban Heat Island are few. Among them, two are of note, one in Granada, Spain (30), using ground stations, and one based on satellites measurements over hundreds of large cities in China (29). In both cases, the dynamic is similar: 6 to 10 hours after sun dawn, the UHII reaches its minimum (classically 0.5 K). This *cooling* part of the cycle is explained by the fact that the city mass absorbs incident heat. Then, the UHII raises to its maximum (given by Eq. 10, for example) in about 5 hours and stabilizes overnight. In this work, UHII(t) was modeled using these

three phases. Mathematically, they are described as a downward cosine, an upward cosine, and a plateau (see Appendix A). While simplistic, this model is capable of reconstructing 4 of the 5 five daily temporal dynamics identified by Lai *et al.* (29) (the standard-spoon, the weak-spoon, the inverse-spoon, and the straight-line).

With the UHII evolution over the day modeled, the question of the rural area temperature comes next. Luckily, it was modeled by Gallo for both clear sky and cloudy weather in an attempt to complement satellite data whenever they are not available (*e.g.*, overcast sky)(31). Using data from 14 American meteorological stations, the authors concluded that two main factors were ambient air temperature ($T_{Air,Out}$) and sky cover (CC). They produced two correlations, one for each condition, linking land surface temperature and ambient air temperature. They are blended here as their average weighted by the cloud cover (CC, from 0 - clear sky - to 1 - overcast sky -) in this work (Eq. 11).

$$\begin{aligned} T_{Rur} = &(1 - CC)(2.82 + 1.15 T_{Air,Out}) \\ &+ CC(1.33 + 1.00 T_{Air,Out}) \end{aligned} \tag{11}$$

Once the surrounding temperature has been modeled, the next step is to describe the absorbed radiation. Here again, the Stefan-Boltzmann formula was chosen for both terms (Eq. 12 and 13). The interfaces reflectivities were determined with the previously introduced procedure (cosine distribution and Eq. 3). The view factor with the surrounding was chosen as the complement to the sky view factor ($F_{Sur} = 1 - F_{Sky} = 0.5$), and the surrounding emissivity was set at 0.9 (ϵ_{Sur}).

$$\Phi_{Sur,Abs} = F_{Sur}\tau_{Sur,Abs}\sigma\epsilon_{Sur}T_{Sur}^4 \tag{12}$$

The final element to account for is the thermal radiation emitted towards the surrounding. Only limited information is available on how to model such a term. Therefore, the classical Stefan-Boltzmann formula was chosen (Eq. 8), with a microalgae suspension emissivity (ϵ_{mc}) taken as 0.9.

$$\Phi_{Sur,Emi} = F_{Sur}\tau_{Sur,Emi}\sigma\epsilon_{mc}T_{mc}^4 \tag{13}$$

3 4. Indoor radiation

The last radiative transfer to be accounted for is the exchange between the microalgae biofaçade and the indoor of the building. Absorbed and emitted radiations are modeled in the same manner as the former fluxes (Eq. 14 and 15). For both, the view factor is chosen as 1.0. The only question is the emissivity of the building interior (ϵ_{In}). This value is quite complicated to evaluate as various types of paints, furniture, and interior layouts can be encountered. Still, indoor emissivity is one of the main factors controlling thermal comfort (which increases with surface emissivity) and building thermal performances (which decrease with surface emissivity). Hence, a trade-off value of 0.6 was chosen, which ensures adequate thermal comfort and energy efficiency (32). Finally, the interfaces reflectivities (leading to transmittance) were assessed assuming a cosine distribution for the incident heat

flux.

$$\Phi_{In,Rad,Abs} = \tau_{In,Rad,Abs}\sigma\epsilon_{In}T_{In}^4 \qquad \textbf{(14)}$$

$$\Phi_{In,Rad,Emi} = \tau_{In,Rad,Emi}\sigma\epsilon_{mc}T_{mc}^4 \qquad \textbf{(15)}$$

3 5. Indoor convection

In addition to radiative exchanges, the system's temperature is also governed by convective fluxes. Indoor convection, like radiation, is not straightforward owing to the multiple possible configurations. Luckily some authors tackled the questions of both free and forced spatially averaged convection coefficients in indoor environments. While far less detailed than usual Nusselt number correlations, they have the advantage of being derived from actual configurations. Clarke compiled several of them in his textbook (14) and pointed out Khalifa and Marshall's work as an adequate choice for free convection evaluation (33). To lead their work, the authors deployed tests in an actual room ($2.95 \times 2.35 \times 2.08$ m^3 in length $\times$ width $\times$ height, yielding a height of 2.08 m used are reference). Sadly, they did not scale their correlations to this volume. Hence, this work uses a slightly modified version of the one they proposed for a wall with no radiator below (Eq. 16, with the applied scaling).

$$h_{In,Conv,Free} = 2.04\,(\frac{H_{mc}}{H_{Ref,In}}(T_{pmma,In}-T_{Air,In}))^{0.23} \qquad \textbf{(16)}$$

Indoor forced convection was assessed using a classical correlation for air at room temperature. The velocity value (U_{In}) was chosen as 0.1 m/s as it corresponds to a velocity classically induced by air renewal in an office environment (32). The characteristic was taken as the average between the height and the width of the system ($L_{Ref} = (1+4)/2 = 2.5$ m). Hence, the Reynolds number has a value of 13500, concluding in a laminar flow. Thus, Equation 17 was used to obtain the averaged convective heat transfer coefficient. Finally, to determine which of the mode was at play, both were evaluated, and the one yielding the highest value of convective heat transfer coefficient was retained.

$$h_{In,Conv,Forced} = \frac{k_{Air}}{L_{Ref}}\,0.664\,Re_{Ref}^{1/2}Pr^{1/3} = 0.72\ \text{W/m²/K} \qquad \textbf{(17)}$$

Still, one has to bear in mind that indoor air is not directly in contact with the culture. A 1.5 cm thick PMMA glazing holds the liquid. Therefore, the question of thermal transfer within this plastic medium has to be addressed. First, one can evaluate its thermal homogeneity by evaluating the Biot number. For a temperature difference of 1 K between the surface and the indoor air, $h_{Conv,In,Free} = 2.4$ W/m^2/K (incidentally dominating the convective transfer), which leads to a Biot number of 0.19. This value, which is an optimistic assessment, is above 0.1. Hence, the system cannot be considered homogeneous from a thermal point of view. Therefore, the thermal resistance of the PMMA glazing has to be con-

sidered in the model. To do so, a thermal resistance in series model was used to properly assess the convective-conductive heat flux between the microalgae culture and the indoor air (Eq. 18).

$$\Phi_{In,Conv,Net} = \frac{T_{Air,In}-T_{mc}}{\dfrac{1}{h_{In,Conv}}+\dfrac{e_{pmma}}{k_{pmma}}} \qquad \textbf{(18)}$$

3 6. Outdoor convection

The contributions of outdoor convective-conductive heat fluxes were dealt with using the same methodology as its indoor counterpart. First, free convection was assessed using a correlation established for vertical flat plates. Among the numerous possibilities, one accounting for both laminar and turbulent regimes was used (Eq. 19)(34). As it yields an averaged value over a distance, it was differentiated to get the value at the system elevation ($E_{mc} = 20$ m). The convective heat transfer coefficient was then compared to the one induced by the wind to retain the largest one.

$$\overline{h_{Out,Conv,Free}} = \frac{k_{Air}}{E_{mc}}\left[0.825+\frac{0.387\,Ra_L^{1/6}}{[1+(0.492\,Pr)^{9/16}]^{8/27}}\right]^2 \qquad \textbf{(19)}$$

Accessing the convective heat transfer coefficient on a building façade is not an easy task. It raises numerous questions, such as wind velocity and orientation, the orientation of the façade (windward or leeward, which can change in time), and the location of the thermal sensors on the façade (center or side, bottom or top). For all these reasons, the numerical assessment of Defraeye *et al.* was chosen as reference in this work (35). In their study, the authors simulated by CFD the heat transfer around a building and proposed a correlation yielding surface averaged convective heat transfer coefficient as a function of wind velocity and orientation (from 0 to 330° with a 30° step). Correlation coefficient are reported in Table 1.

Coming back to the biofaçade wind-induced heat transfer assessment, the evaluation process starts by comparing the wind direction, is given by meteorological data, to the façade orientation to obtain the incidence angle (θ_{Wind}). Then, meteorological velocity (evaluated at an elevation $E_{Station} = 10$ m) is corrected according to Defraeye advice (Eq. 20, $r_{Station}$ and $r_{Station}$ being the surface roughness near the meteorological station and the building, taken as 0.3 am) to obtain the velocity at the microalgae biofaçade elevation ($E_{mc} = 20$ m). Consequently, the convective heat transfer coefficient is evaluated using Defraeye's correlation for the two incidence angles surrounding the actual one (Eq. 21 with coefficients in Table 1). Ultimately, the obtained values are linearly interpolated to obtain the value for the exact wind incidence angle on the biofaçade at a given time.

Wind incidence angle (θ_{Wind}, in degree)	$A_{\theta_{Wind}}$ (W/m^2/K)	$B_{\theta_{Wind}}$ (-)
0	4.90	0.86
30, 330	4.63	0.87
30, 300	4.25	0.88
90, 270	2.78	0.87
120, 240	1.44	0.83
150, 210	1.85	0.84
180	2.25	0.84

Table 1. Defraeye's correlation for different wind incidence angles on the façade. Couples of incidence angles tied to the same parameters originate from symmetry consideration

$$U_{Out} = U_{Station} \left(\frac{r_{Building}}{r_{Station}} \right)^{0.0706} \frac{\ln(\frac{E_{mc} + r_{Building}}{r_{Building}})}{\ln(\frac{E_{Station} + r_{Station}}{r_{Station}})} \tag{20}$$

$$h_{Out,Conv,Forced} = A_{\theta_{Wind}} U_{Out}^{B_{\theta_{Wind}}} \tag{21}$$

Finally, the thermal resistance of PMMA glazing and the potential second layer creating double glazing was described using thermal resistance in series model (Eq. 22).

$$\Phi_{Out,Conv,Net} = \frac{T_{Air,Out} - T_{mc}}{\frac{1}{h_{Out,Conv}} + \frac{n_{Glaz} e_{pmma}}{k_{pmma}} + \frac{(n_{Glaz} - 1) e_{Air}}{k_{Air}}} \tag{22}$$

3 7. Gas flow power

The last source of thermal energy to be accounted for is the energy carried by the gas sparged into the culture. This gas ensures two key aspects of a microalgal cultivation process: gas exchange (carbon dioxide supply and oxygen removal) and mixing. This gas flow rate is classically expressed in Vessel Volume per Minute (for VVM). In this work, a typical value of 0.2 (f) was chosen. Assuming that the sparged gas reaches thermal equilibrium before reaching the top of the biofaçade (4 m), and considering the gas to have the physical properties as air, the net thermal power influx can the written as in Equation 23, where T_{Gas} is the sparged gas inlet temperature.

$$P_{Gas,Net} = f H_{mc} w_{mc} e_{mc} \rho_{Gas} C p_{Gas} (T_{Gas} - T_{mc}) \tag{23}$$

3 8. Resulting thermal dynamic

Finally, the temporal dynamic of the microalgae culture can be computed by summing all the heat fluxes at stake in the thermal balance of the system (Eq. 3.8). Two additional assumptions are drawn to establish this balance: the gas-induced mixing is considered intense enough to ensure a uniform temperature in the cultivation compartment, and the culture has the same thermal properties as water. The last question to be addressed is the initial condition of the system. It

was set as the indoor temperature (22 °C, US Occupational Safety and Health Administration advises between 20 and 24.5 °C (36)).

$$H_{mc} w_{mc} e_{mc} \rho_{Water} C p_{Water} \frac{dT_{mc}}{dt} =$$
$$H_{mc} w_{mc} [\Phi_{Sun,Abs} + \Phi_{Sky,Abs} \Phi_{Sky,Emi} + \Phi_{Sur,Abs}$$
$$- \Phi_{Sur,Emi} + \Phi_{In,Rad,Abs} - \Phi_{In,Rad,Emi} + \Phi_{In,Conv,Net}$$
$$+ \Phi_{Out,Conv,Net}] + P_{Gas,Net}$$

4. Biological model

Once the thermal dynamic of the system has been computed, its impact on the microalgae culture is to be evaluated. Models accounting for the impact of temperature on microalgae growth have been reviewed by Bechet *et al.* (37). His work pointed toward a parametrization of the Cardinal Temperature Model with Inflection (polynomial fitting of cell growth rate at different temperatures, Eq. 24) (38). For this work, the model was parametrized using data obtained by Mayo for *Chlorella vulagris* (19). The resulting growth is graphed in Figure 2. Three qualitative parts of the curve were drawn. The first one, in blue ($T_{mc} < 17.7$ °C), is deemed too cold as the growth rate is below 75 % of the optimal value. The second one, in green ($17.7 \leqslant T_{mc} < 39.9$ °C), is considered adequate. The last one, in red (39.9 °C $\leqslant T_{mc}$), is flagged as dangerous as the growth rate drops below 75 % of the optimal value because of overheating. Finally, one last range of temperature was considered in this work as it is also dangerous to the system and induces a fatality to the cells: the sub-zero condition.

On top of temperature, another parameter is key: light, as it drives photosynthesis, hence the system's productivity. The incident light is obtained by summing the one coming directly from the sun ($\Phi_{Sun,Vis}$) and the one coming from the sky ($\Phi_{Sky,Vis}$). Still, as the microalgal cells will absorb this light, the incident value does not inform of the light availability within the culture. This quantity will be approached using the aforementioned assumption that culture cell density is controlled so that a desired fraction ($\alpha = 0.5$) of the green radiation is transmitted. This assumption also allows computing the volume average photosynthetically active light intensity, $\bar{I}$ as a function of incident light intensity, I_0 (given by $\Phi_{Sun,Vis} + \Phi_{Sky,Vis}$), using Equation 25 (assuming exponential decay of incident light and that microalgae adsorb

$$\mu(T_{mc}) = \mu_{Max} \frac{(T_{mc} - T_{Max})(T_{mc} - T_{Min})^2}{(T_{Opt} - T_{Min})[(T_{Opt} - T_{Min})(T_{mc} - T_{opt}) - (T_{Opt} - T_{Max})(T_{Opt} + T_{Min} - 2T_{mc})]} \tag{24}$$
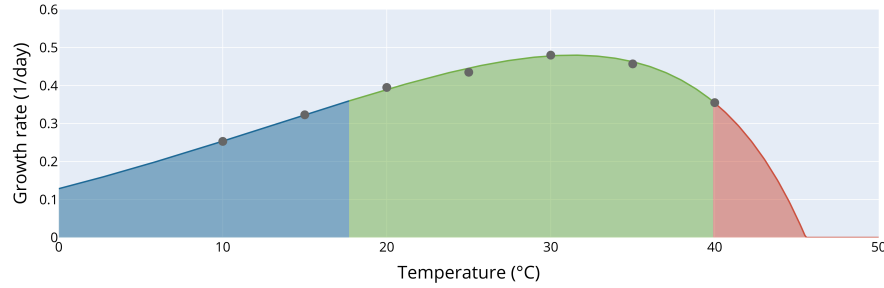

Fig. 2. Growth rate reconstruction by the Cardinal Temperature Model with Inflection for *Chlorella vulgaris*. Markers - experimental points from (19). Blue area - range deemed too cold to adequately lead the microalgae culture. Green - optimal range. Red - too-hot range

twice more efficiently red and blue light than green light (21)). In accordance with several reports for *Chlorella vulgaris* cultures in tightly controlled light condition (18, 39), a threshold value of 150 μmolPhotonPAR/m^2/s was retained as performance indicator. Below this value, the culture is considered light-deficient, above it is considered light-sufficient. The two last questions that can come to the reader's mind are the intermittency of the light experienced by the cells and a potential excess of light. As for the first one, cells will be shuttled from light to dark zones, and vice-versa, by the fluid flow. Yet, recent work showed that their physiological response is not different from the one under continuous light, at least up to 800 μmolPhotonPAR/m^2/s (18). Furthermore, when adequately cycled between light and dark zone (as in this system), cells can handle illumination up to 7000 μmolPhotonPAR/m^2/s, corresponding to 3.5 times the illumination at midday in summer, which is quite unlikely to occur naturally (17). Therefore, those two last concerns can therefore be ruled out.

$$\overline{I} = \frac{I_0(\alpha^2 + \alpha - 2)}{3\ln(\alpha)} \tag{25}$$

5. Weather data

The meteorological data powering the model were obtained from Météo-France (the public French weather forecast agency). The whole set covers France, with about one station per administrative region. Data span from 1996 to date, with a measurement every 3 hours. The reported parameters are numerous. Only the ones relevant to this model are reviewed here. From this extensive dataset were extracted: air temperature, cloud cover, wind (at 10 m above the ground) velocity, wind direction, relative humidity, and static pressure (to compute gas density, ρ_{Gas} in Eq. 23). The database was accessed on April 2023.

Among the possible spatial locations and time spans, the year 2020 in Marseille, France, was chosen for demonstration. Three reasons pointed toward this choice. First, the years 2021 and 2022 were exceptionally hot in France. Thus, they may not be faithful representatives of nominal system behavior. Second, Marseille is a city located in the South

of France, where solar resource is abundant. As a microalgae cultivation process is driven by photosynthesis, it was assumed that this type of place was the most relevant. Finally, analyzing system performance over several years would unnecessarily lengthen this article which is focused on the thermal behavior of the system and its optimization. Therefore, only one year was simulated.

6. Numerical parameters and physical assumptions validation

Once implemented (Python 3.9), the model was used to simulate a reference case: a South-oriented biofaçade located in Marseille, France, over the course of the year 2020. The values of the parameters associated with this case are available in Table 2 for system configuration parameters, in Table 3 for physical, radiative, and biological parameters, and in Table 4 for operating conditions.

Before diving into the dissection of the behavior of the biofaçade, it was important to verify that numerical parameters had a negligible impact on the results. The first parameter to be controlled is the timestep for the integration. Timesteps from 0.01 to 3 h (meteorological data frequency) were tested. A clear convergent trend was observed as the timestep was reduced. A maximum deviation of 1 % on the model predictions was deemed a sufficiently strict criterion, especially compared to the effect of the uncertainty associated with uncertain parameters (see below). Consequently, a timestep of 0.5 h (30 minutes) was selected.

With this value, it is possible to assess the validity of using the thermal resistance in series model. Indeed, this model is valid if the thermal transfer achieves a steady state. In this case, the timestep is to be compared to the characteristic times for air and PMMA, 3 seconds and 8 minutes, respectively. With a timestep three times higher than the highest of these values, the use of the thermal resistance in series model is fully justified.

The last question to be addressed was the duration of the transient period to be discarded at the beginning of the simulation to ensure no effect from the initial condition (44). Transient periods up to 60 days were tested. The tests revealed that the duration influenced by the initial condition

Symbol	Description	Value	Unit
E	Elevation of the biofaçade above the ground	20	m
$E_{Station}$	Elevation of the velocity sensor of the meteorological station	10	m
e_{air}	Air thickness (double galzing only)	0.015	m
e_{mc}	Thickness of the biofaçade reservoir	0.05	m
e_{pmma}	PMMA walls thickness	0.015	m
H_{mc}	Height of the biofaçade	4	m
$H_{Ref,In}$	Reference height for Khalifa's correlation	2.08	m
L_{Ref}	biofaçade reference length	2.5	m
n_{Glaz}	Number of outdoor glazing	1	-
$r_{Building}$	Roughness in the biofaçade surrounding	0.3	m
$r_{Station}$	Roughness in the meteorological station surrounding	0.3	m
w_{mc}	Width of the biofaçade	1	m

Table 2. Parameters describing biofaçade configuration in the reference case

Symbol	Description	Value	Unit
Cp_{Air}	Air specific heat	1004	J/kg/K
Cp_{Water}	Water specific heat	4183	J/kg/K
F_{Sky}	Sky view factor†	0.5	-
F_{Sur}	Surrounding view factor (= 1 - F_{Sky})	0.5	-
k_{Air}	Air thermal conductivity	0.026	W/m/K
k_{pmma}	PMMA thermal conductivity (40)	0.18987	W/m/K
Pr	Air Prandtl number	0.71	-
U_{In}	Indoor air velocity†	0.1	m/s
ϵ_{In}	Indoor emissivity†	0.6	-
ϵ_{mc}	Microalgae culture emissivity†	0.9	-
ϵ_{Sur}	Surrounding emissivity†	0.9	-
ζ_{Air}	Air refractive index (41)	1.00028276	-
ζ_{mc}	Microalgae culture refractive index (42)	1.339	-
ζ_{pmma}	PMMA refractive index (43)	1.5082	-
ν_{Air}	Air kinematic viscosity	$1.85\ 10^{-5}$	m²/s
η_{ps}	Photosynthesis efficiency (10)	4.34	%

Table 3. Physical, radiative, and biological parameters. † parameter varied during the sensitivity analysis

Symbol	Description	Value	Unit
α	Green light transmitted fraction	0.5	-
f	biofaçade aeration	0.2	VVM
T_{Gas}	Sparged gas temperature (= $T_{Air,In}$)	22	°C
$T_{Air,In}$	Indoor temperature	22	°C

Table 4. System operating conditions in the reference case

was below 1 day. It can be explained by the fact the simulation starts at 1 am on the 1st of January assuming the biofaçade is at the same temperature as the building hosting it. It positions the system close to its average value and leaves it some time to equilibrate before sun dawn. Anyway, a transient period of seven day was selected, as exploring possible designs might slightly modulate this conclusion.

7. Results

Once confidence in the numerical procedure has been established, the model could be used to explore the system dynamics. First, the overall behavior is presented. Yet, as it represents a large quantity of data, performance indicators were computed in order to ease analysis and interpretation. One should note that night periods were excluded from the con-

struction of the performance indicators (except for sub-zero temperatures) as microalgae would obviously not perform photosynthesis in the dark. Determining daytime requires the choice of a criterion. Gallo suggested an experimental one: an incident solar heat flux higher than 25 W/m^2 (31). Yet, it raises the question of the orientation of the surface receiving the heat flux surface and potential interferences from clouds. In this work, the solar altitude (provided by the illumination model) was chosen. A positive solar altitude was considered as marking daytime. This approach conveniently alleviates the problem of potential could cover interference.

7 1. Daily basis analysis: illumination and temperature histories

Figure 3 presents the dynamics of the system in terms of thermal and illumination histories. First of all, the culture compartment temperature ranges from 1.8 to 40.1 °C, with an average value of 17.9 °C, close to the indoor building temperature. Second, it varies strongly over the day/night cycle, like the outer air temperature. Yet, its amplitude is exacerbated, especially during the cold season. This last distinction is important. Indeed, in order to dive further into the examination of the system dynamics, two patterns have to be ac-
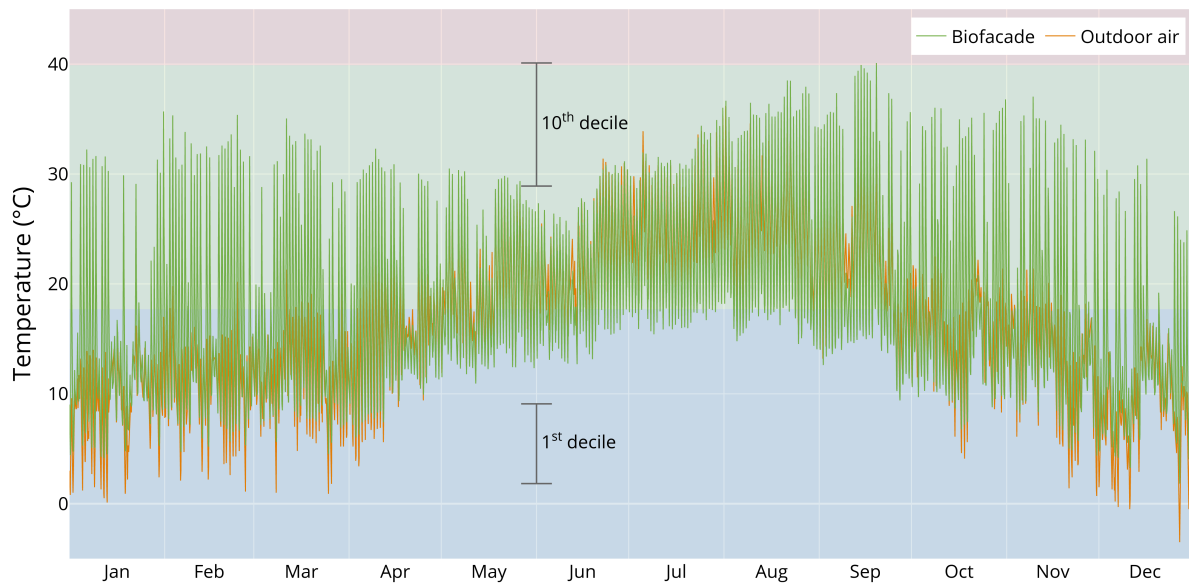
(a) Temperature history
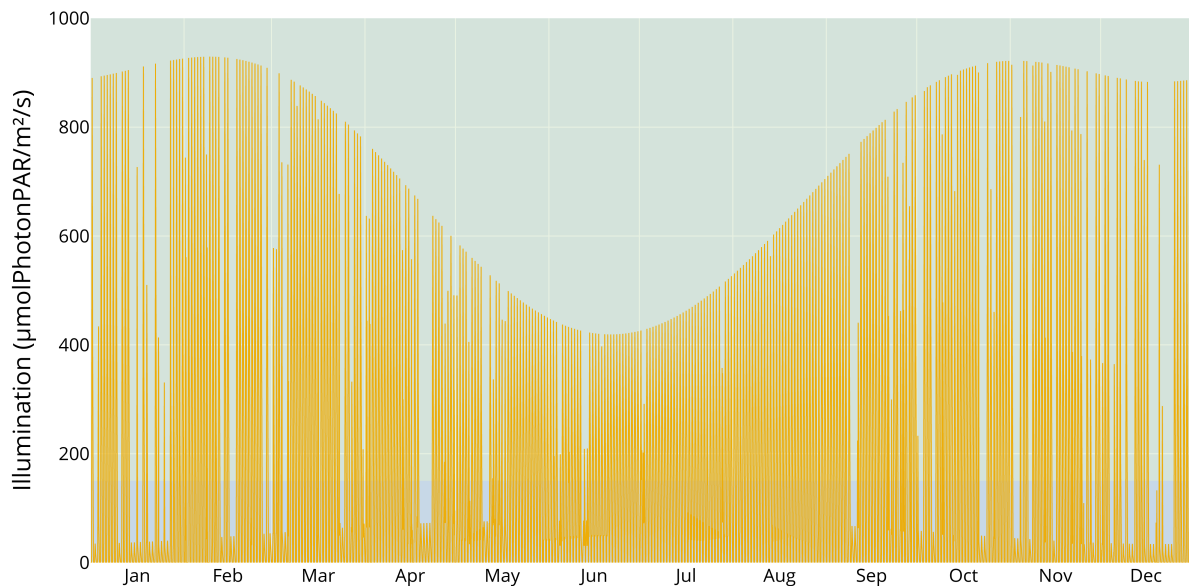
(b) Incident visible light history

Fig. 3. Temporal dynamics for a reference case biofaçade located in Marseille, France, oriented towards the South over the year 2020. Shaded areas in the background: blue - too low temperature or too low illumination, green - adequate temperature or adequate illumination, red - too high temperature

knowledged: one for the cold season (November to March) and the other for the hot season (April to October).

During the cold season, on sunny days, the system daytime temperature is much higher than its outdoor counterpart (+15 °C), while the nighttime temperature is a few degrees below the latter (-2 °C). The subsequent increase in temperature during the daytime allows the microalgae culture to enter a productive state despite adverse outdoor conditions. This trait of biofaçade represents an undeniable improvement over other types of outdoor photobioreactors, which must be halted during the cold season (45). On cloudy days, the biofaçade temperature is only a few degrees higher than the outdoor air. This could potentially limit cell growth if only sufficient light

was available.

During the hot season, the magnitude of the thermal day/night cycle is attenuated. While one could have expected an excessively hot temperature, it is only encountered once (the mid-September event analyzed below). This counterintuitive behavior can be explained by the vertical orientation of the biofaçade. Thus, as solar altitude increases during the hot season, the incident radiation coming from the sun decreases (Fig. 3 b). Nevertheless, this decrease in incident radiation is not marked enough to hinder cell photosynthesis during the period. Hence, unsurprisingly, this moment of the year represents the most suitable time for microalgae cultivation.
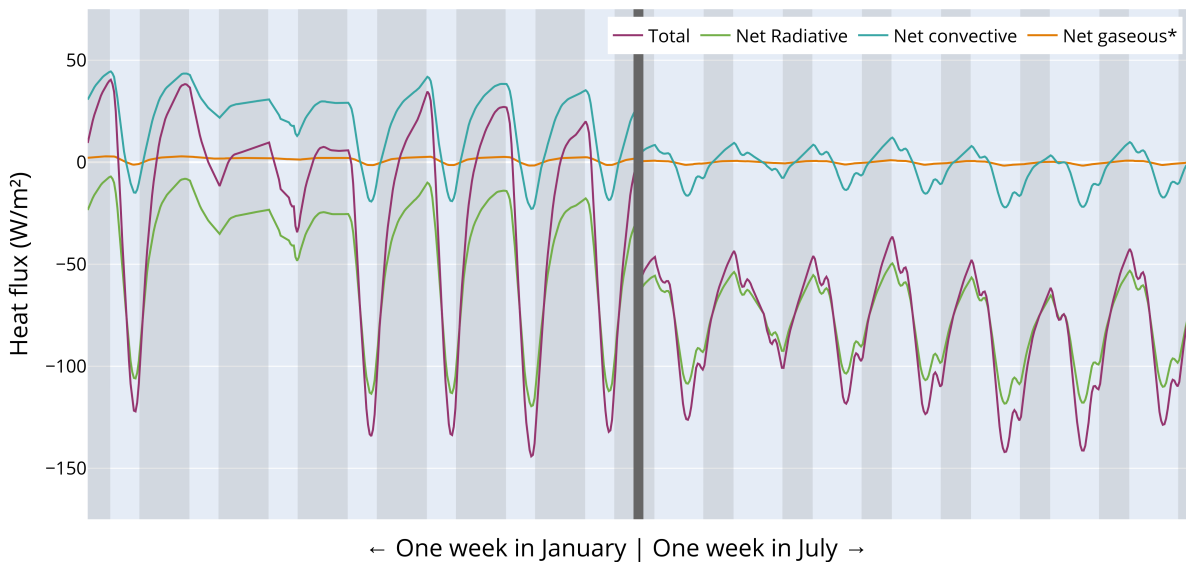
Fig. 4. Net heat flux exchange between the biofaçade and the host building. On the left, a week during the cold season, on the right, a week during the hot season. * gas power was divide by $H_{mc}w_{mc}$ before being drawn on this chart

7 2. Hourly analysis: biofaçade / host building interaction

The model reveals another difference between the cold and hot seasons: the thermal interplay between the biofaçade and its host building (Fig. 4). The two parts of system can exchange heat via three mechanisms: convection, radiation, and heat conveyed by the gas (from the host building to the biofaçade only). As one can see, the power supplied to the host building to the biofaçade by the sparged gas is negligible before the two others. Among the two remaining, the net radiative heat flux is consistently negative, meaning that the biofaçade suffers a net loss of thermal energy by this mode of transfer. This observation is explained by the different emissivities of the mircoalgae culture (0.9) and the building inner surface (0.6), resulting in a radiative temperature consistently higher for the microalgae culture.

On the contrary, convective heat exchanges are either positive or negative depending on the hour of the day and the subsequent temperature contrast between the system. While intricated, this interplay can be simplified into three patterns:

- During the cold season, under a clear sky, the biofaçade heats up the building during the day while the building transfers back its power at night. This is a clear synergy: increasing thermal comfort over daytime, preventing biofaçade sub-zero temperatures during nighttime.

- During the cold season, under a cloudy sky, the net total heat exchange fluctuates around zero. Here, the system stabilizes naturally to a compromise: not fostering thermal comfort and limiting the temperature drop of the culture.

- During the hot season, the biofaçade continuously transfers heat to its host building. In this case, the in-

teraction is not favorable to the building (assumed sufficiently hot already) and only benefits the biofaçade by preventing its overheating.

### 7 3. Acute event analysis: mid-September event

The model hourly resolution not only allows for deciphering the interplay between the biofaçade and its host building, but it also offers a great tool to explore in-depth acute events such as the mid-September overheatings (September 13rd to 15th and 19th). During this period, France was facing a heat wave. Hence the first explanation that could come to one's mind could be simple: the overheating happening during the late stages of the day the Urban Heat Island must be responsible for it. The actual explanation is more complex.

Figure 5a displays the temperature histories of the system over the second and third weeks of September 2020. As one can see, the biofaçade surrounding temperature is quite hot (around 38 °C) over the event. Furthermore, the Urban Heat Island Intensity is peaking (up to +4 °C), and the resulting surrounding temperature can exceed 40 °C. Yet, a careful observer will note that the culture overheating is somewhat delayed and does not coincide with the surrounding temperature peak. Hence, while undeniably contributing to the system overheating, scorching surrounding air and intense Urban Heat Island phenomenon do not lead to excessive culture temperature alone. Indeed, the temperature difference between the biofaçade and its surroundings drives a net heat loss for the microalgae culture. Diving further into the heat balance of the system is therefore required to understand the underlying mechanism.

Figure 5b presents heat fluxes contributing to the thermal balance of the microalgae reservoir, which are not mediated by the surrounding temperature: absorbed sun and net sky radiative heat flux. The net convective heat loss is also displayed to analyze if the overheating could be linked to an
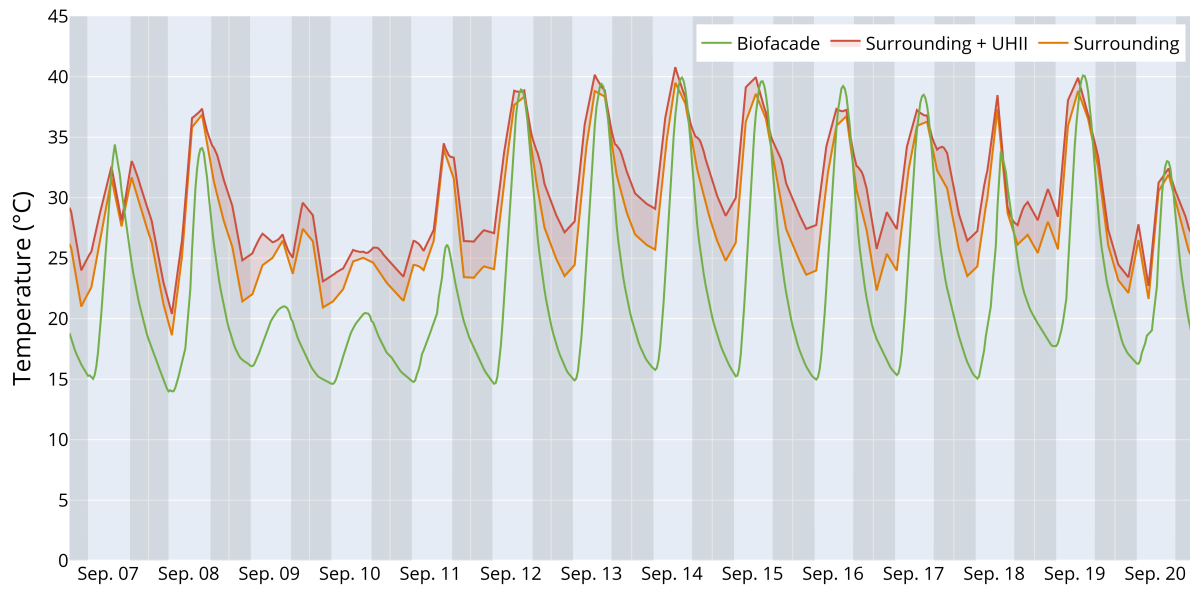
(a) Temperature history
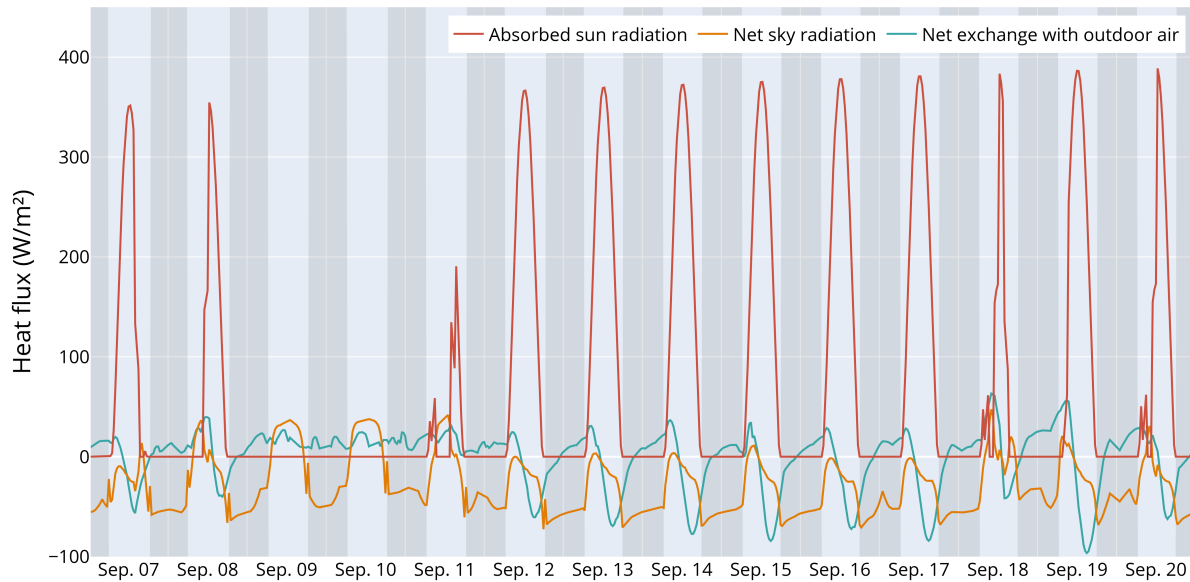
(b) Absorbed heat flux

Fig. 5. Hourly dynamic of the biofaçade over the second and third week of September

exceptionally low convective heat flux from the biofaçade to its surrounding (because of the lack of wind, for example). A glance shows that the explanation based on the convective heat loss can be ruled out, leaving only the sun and the sky radiations as potential explanations. During the overheating hours, the absorbed solar heat flux is around 250 W/m² (sharply declining, though), and the net sky radiative heat flux exhibits a shoulder around -20 W/m² extending for a few hours. Combined together, and accounting for the microalgae culture thermal inertia, they lead to a temperature increase of 2 °C over 30 minutes. Thus, it is their contributions that explain how the biofaçade enters the dangerously hot zone. Deciphering so intricated mechanisms is only possible using a model and highlights the complexity of a biofaçade system. It

also underlines the relevance of systematic experimental approaches, which better capture interacting parameters, such the one deployed by Umdu (4).

7 4. Limitations

While the model can decipher the interplay between key phenomena contributions, it also suffers limitations. Going from outdoor to indoor, the major limitations can be discussed. First of all, the building hosting the biofaçade is assumed to have clear access to the solar resource. This implies that no taller building cast its shadows onto the façade. This can, of course, be the case, but from a city layout perspective, it implies that not all buildings will be eligible for a biofaçade implementation. Another specificity of the model that hinders

its generalization is that the studied system is designed as a glazing. Therefore, it can either be deployed during the construction of the building or an extensive renovation involving glazing replacement. The model should consequently be adjusted (marginal amount of work) for double skin implementation.

Regarding the system itself, it is assumed to work at its nominal capacity constantly. Yet, a biological system can be the place for the development of a biofilm colonizing the glazing surface. If so, the optical transmission would be lowered, and the captured power would increase. Its phenomenon could be considered as a refinement of the model or prevented as simple technical measures can effectively manage it (*e.g.*, adding rubber beads to scrub the biofilm off the glazing). In addition, the overall confidence in the model could be enhanced by producing a demonstration unit. The goal would be to validate the system's thermal behavior, followed by the biological aspects.

Furthermore, the interaction with the building is modeled assuming constant temperature and heat convection coefficient on the building side. These assumptions do not align well with the indoor atmosphere, which fluctuates over the day and year.

8. Performance indicators

Accessing the hourly dynamic of the system is extremely valuable and helps to pinpoint and explain specific events (*e.g.*, mid-September overheating). Nevertheless, this wealth of information may become a burden when it comes to having a synthetic overview of the system's performances, especially if one would like to compare several configurations. Consequently, the daytime operation (solar altitude above 0°, 4412 hours in total) will be divided into six categories: (light-deficient or light-sufficient) × (too-cold, adequate, or too-hot temperature). Potentially freezing temperatures (during the winter nights) were also tracked over daytime and nighttime as they would induce an additional operational constraint. Furthermore, the first and tenth deciles (and their spreads) of the microalgae culture temperature distribution are also considered valuable indicators as they provide information on the occurrence and intensity of extreme events.

Figure 6 provides a graphical synthesis of these performance indicators. The temperature distribution exhibits two modes: a cold one (around 17 °C) and a hot one around (28 °C). Their relative importance is reflected in the classification, with 38.9 % of the time deemed too cold and 61.0 % deemed adequate from a thermal point of view. Finally, the daytime fraction featuring adequate temperature and illumination represents 41 % of the total daytime. This value can be regarded as high. Indeed, the chosen criterion to evaluate daytime (solar altitude above 0°) is quite broad and necessarily features moments (sunrise and fall) when the incident light cannot meet the culture demand. Finally, the first and tenth deciles (values and spreads) do not exhibit extreme events, apart from the mid-September event. Further in-depth analysis of performances and how design choices affect them is dealt with specifically in the companion paper (46).
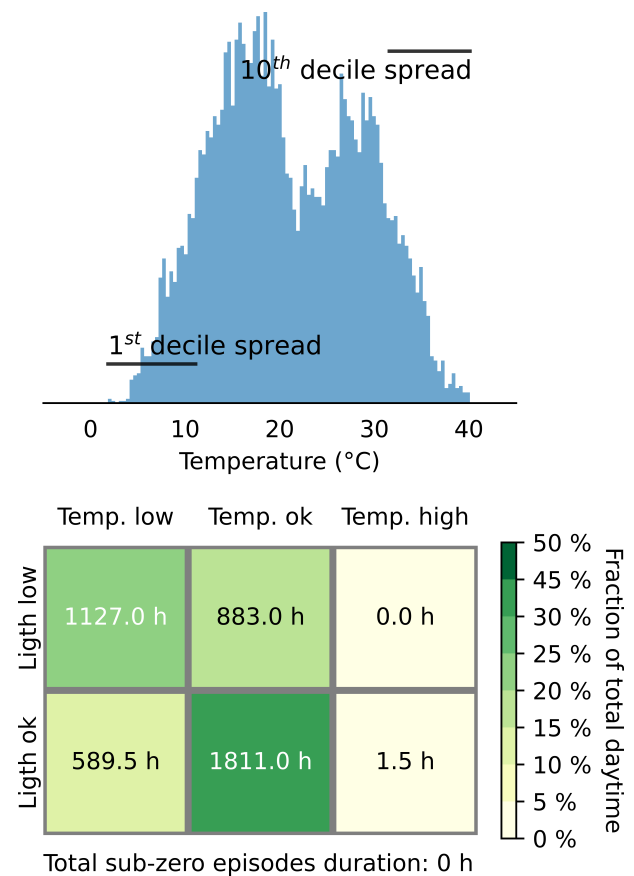

Fig. 6. biofaçade performance indicators. Top - temperature distribution over daytime. Bottom - daytime operating hours repartition

9. Sensitivity analysis

Obtaining a functional model and evaluating its capabilities is only the first step before using it to explore microalgae biofaçade design. Before using it, one must critically examine its weaknesses and their magnitudes. Three can be spotted in the case of this model: a submodel rising doubts (Urban Heat Island Intensity), parameters for which uncertainty is high (microalgae culture emissivity, for example), and the potential impact of major design modifications (using double glazing, for example). This last Section is therefore dedicated to a critical look back on these potential shortcomings.

9 1. Submodel-associated uncertainty

This work introduced a new and relatively simple hourly Urban Heat Island Intensity model. While backed by several articles, the magnitude of this modeling choice is to be assessed. To do so, this submodel was either deactivated or replaced by a constant value of +2 °C. Figure 7 illustrates the effect of the different approaches simulating the Urban Heat Island Intensity. From both a qualitative and quantitative perspective, the impact is minor. Not modeling the Urban Heat Island phenomenon (left) only changes the performance indicators by 5 % at maximum (excluding overheating, yet going from 1.5 to 0.5 hour is deemed negligible). Assuming a constant Urban Heat Island Intensity of +2 °C (right) yields performances extremely close (most deviation below 1 %) to the one delivered by the proposed hourly model. It can therefore

be concluded that the way the Urban Heat Island Intensity is modeled does not have a significant impact on the overall model predictions. This conclusion is all the more true when one compares the deviations associated with the choice of this submodel (tens of hours) to the variations related to the parameters uncertainties (hundreds of hours, next Section).

9 2. Parameter-associated uncertainty

In addition to the uncertainties associated with how some system components are modeled, others arise from the unknown surrounding the parameter values. Indeed, among the various parameters of the model, some are known with great accuracy (PMMA thermal conductivity, for example), while others have a more blurry definition (microalgae culture emissivity, inner air velocity, ...). To analyze their impact, several methods exist. The main ones are sensitivity analyses, which can be local or global. The first type examines the evolution of the output as a function of a slight variation of inputs around well-defined operating conditions. From a mathematical perspective, they consist in computing the derivatives of the model's predictions as a function of the selected parameters. While accurate and fast, they are not able to deliver easy-to-interpret results when the number of uncertain parameters is high.

Consequently, global sensitivity analyses were developed. They examine the influence of selected parameters over a wide range of configurations (by combining the uncertainty of all the selected parameters). In this view, Sobol's indices method stands out for its ease of deployment and interpretation ([47]). In a nutshell, numerous combinations of parameter values are generated (about 120 thousands here), and an ANOVA regression is conducted to determine the amount of variance associated with each of the parameters and their interactions. In our case, the selected parameters and their ranges are presented in Table 5. A uniform sampling approach was used to draw parameter values from the presented intervals before running the model. One should note that using this type of sequence is particularly conservative as extreme configurations are as likely as central ones. Therefore, it ensures the robustness of the conclusions drawn.

Symbol	Description	Range	Unit
F_{Sky}	Sky view factor	[0.4 − 0.6]	-
U_{In}	Indoor air velocity	[0.05 − 0.15]	m/s
ϵ_{In}	Indoor emissivity	[0.5 − 0.7]	-
ϵ_{mc}	Microalgae culture emissivity	[0.8 − 1.0]	-
ϵ_{Sur}	Surrounding emissivity	[0.8 − 1.0]	-

Table 5. Parameters selected for the Sobol's indices analysis and their explored range of variation. Samples drawn following a Sobol sequence

Figure 8 presents Sobol's indices of the different parameters for the main outputs of the simulation. Sobol's indices are ratios of variances; therefore, they weigh the relative contribution of a parameter uncertainty with respect to the overall uncertainty. As they are relative contributions, it is also important to report the absolute variation of the outcome of interest. Therefore, the total variation (standard deviation) induced by exploring the parameter values is also reported
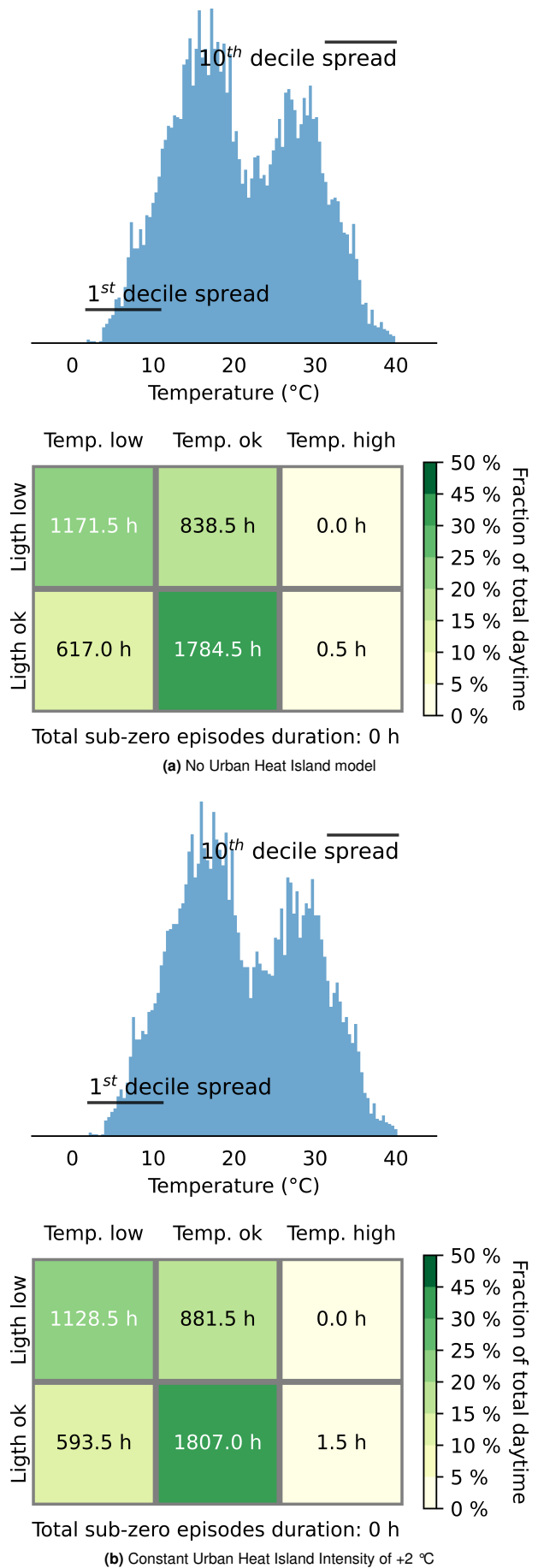

(a) No Urban Heat Island model

(b) Constant Urban Heat Island Intensity of +2 ℃

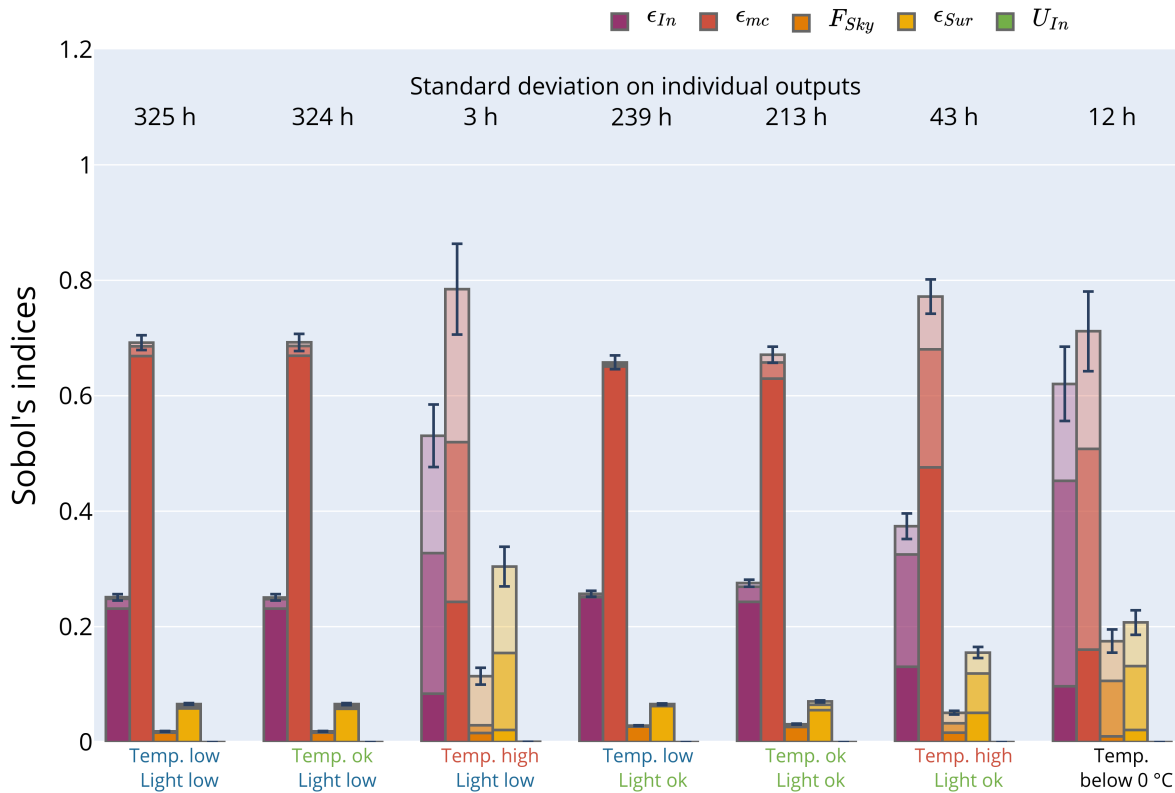**Fig. 7.** Performance indicators for the variations of the Urban Heat Island Intensity model

Fig. 8. Sobol's indices in the reference configuration. Solid bars - first order indices. Shaded bars - second order indices. Almost empty bars - total order with confidence interval

(values on the top of the bars). The first comment is that these variations represent up to 7.4 % of the total daytime (for example, 325 h versus 4412 h for the too-cold and too-dark category). The second comment is that most of the uncertainty originates from two parameters alone (solid bars) and their interaction (shaded bars): the microalgae culture emissivity and the building indoor emissivity. For the main effects, the explanations are straightforward: a decrease of the microalgae culture emissivity leads to an increase in of the temperature of the biofaçade. Hence it lowers the number of low-temperature operating hours while increasing the number of adequate ones. The same mechanisms, in the reversed way, applies to the building's indoor emissivity. The combined effect is at stake for the high-temperature episodes. Indeed, their increase is conditioned by both a rise in indoor emissivity and a fall in microalgae culture emissivity. Finally, the reversed mechanism is responsible for the apparition of sub-zero temperatures.

Three conclusions can be drawn from this analysis. First, the uncertainty tied to parameter values overpasses the one linked to the Urban Heat Island Intensity model. Second, the most influential parameters are those describing the interaction between the biofaçade and its host building. Third, the repartition of the operating time between the six categories can be deemed 7.4 % accurate, which can be deemed relatively good. Indeed, while 7.4 % might seem non-negligible in an engineering system, it is important to note that a biofaçade combines engineering and biological systems. In biology, obtaining predictions that can be deemed 10 % (or be-
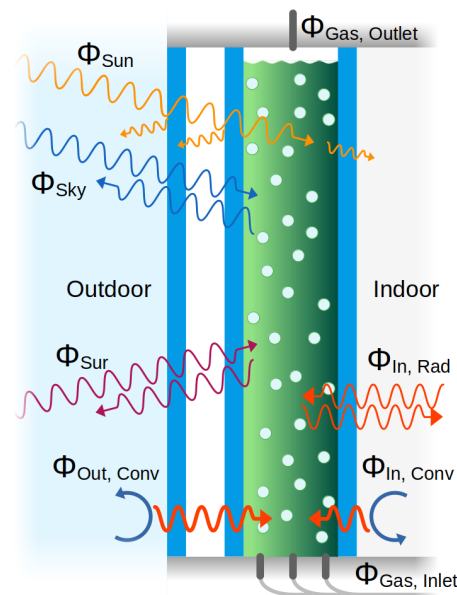

Fig. 9. Schematic representation of the considered microalgae biofaçade with double glazing. The reported heat fluxes (Φ) are introduced in the text
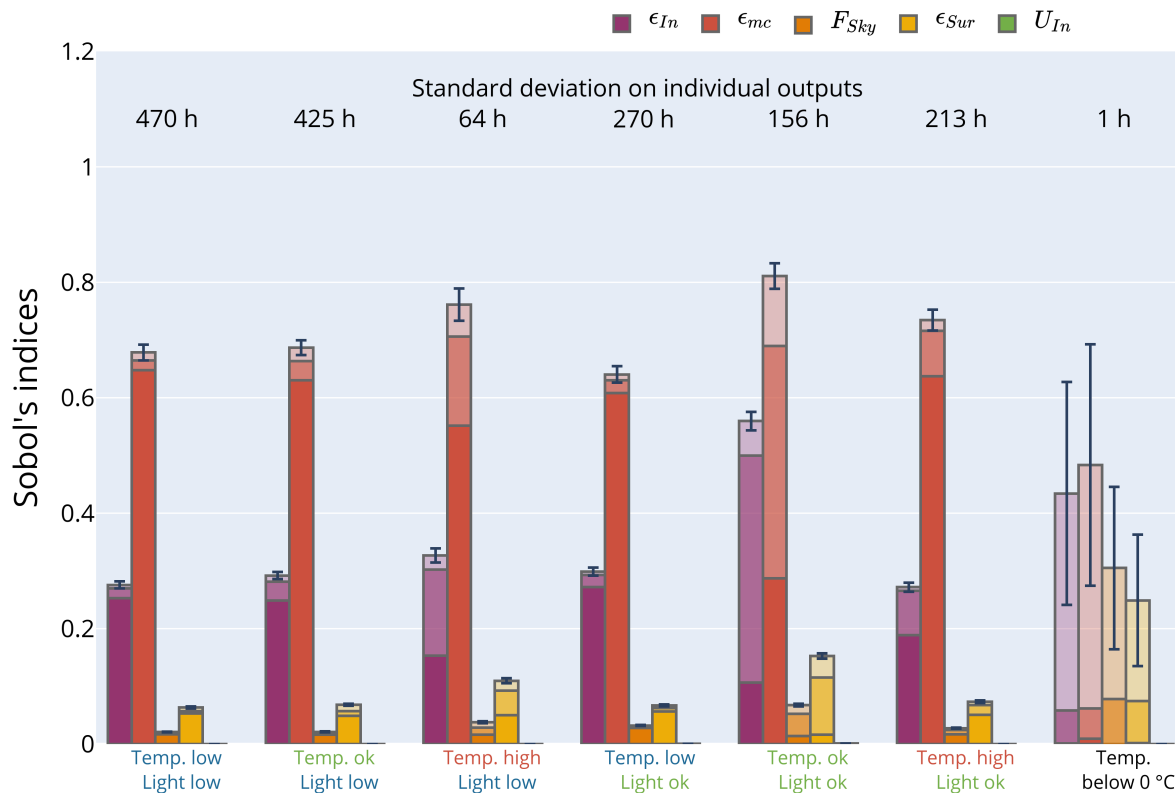
Fig. 10. Sobol's indices in the double-glazing configuration. Solid bars - first order indices. Shaded bars - second order indices. Almost empty bars - total order with confidence interval

low) accurate is very satisfactory.

9 3. Impact of system design

While Sobol's indices analysis explores the impact of selected parameter values, it does not cover important changes in the biofaçade design itself. Among the possibilities (wider microalgae cultivation tank, radiation-selective films (48, 49), ...), the use of double-glazing (Fig. 9) is the most obvious one (4). Yet, this type of change could modulate the conclusions drawn in the previous Section. Hence, the same analysis was performed to assess whether or not the former conclusions relevantly extend over significant design modifications.

Figure 10 presents Sobol's indices and the standard deviations in the case of a biofaçade equipped with an external double-glazing. As one can see, the building's indoor emissivity and the microalgae culture emissivity remain the most influential parameters. Yet, the magnitude of their effect is higher, which relates to the fact that double-glazing favors a transition from too-cold to adequate and from adequate to too-hot temperatures. The observation on the importance of their interplay also stands. In a nutshell, subsequently modifying the design modulates the extent of the previous conclusions but does not hinder their validity. It is, therefore, important to better assess the value of those parameters. First, microalgal suspension emissivity could be measured by dedicated experiments. Selecting a low emissivity strain could be favorable to limit heat loss when the surroundings are colder than the façade (Fig. 3). Second, while little could be done to

change it, a field survey could be led to measure urban emissivity values and their distribution. This action could allow to explore more precisely the impact of this parameter.

10. Conclusion

This article presented the development of a model predicting the thermal behavior of a microalgae biofaçade. Radiative, convective, and conductive heat transfers, modulated by actual weather data, and the biological response were modeled and coupled to yield the most comprehensive biofaçade model to date. After ensuring the convergence of the numerical parameters (timestep, initial transient duration, ...) and validating construction hypotheses, the model was applied to an illustrative case: city of Marseille over the year 2020. Analyzing the results illustrated the model's capabilities: from the dissection of acute events to year-round performance prediction. The numerical behavior of the model was then analyzed: the influence of the Urban Heat Island submodel (for which confidence is low) was investigated, and a global sensitivity analysis (Sobol's indices) was led to assess the impact of uncertain parameters. Even under conservative assumptions, the predictions of the model are 7.4 % of the total daytime accurate. The parameter inducing the highest amount of uncertainty are the microalgae culture emissivity and the building indoor emissivity. Finally, the robustness of these findings was confirmed by testing single vs. double-glazing configurations. Consequently, it is with high confidence that this model can be used, in a companion paper, to design a
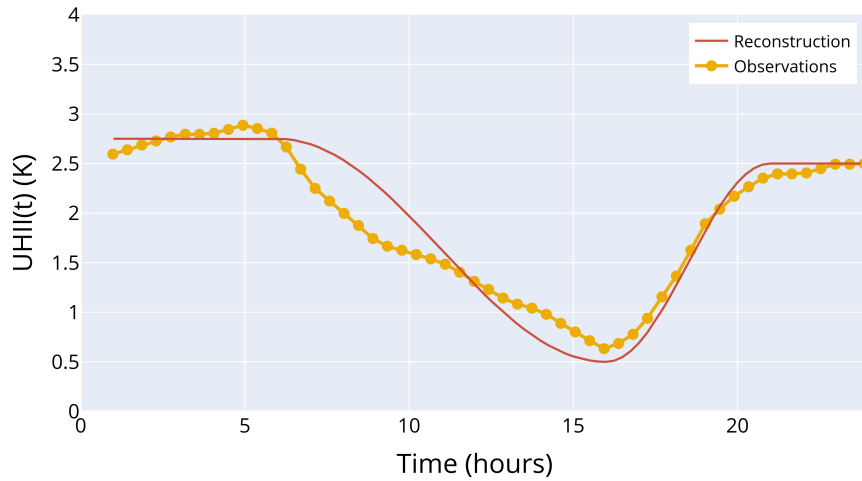
Fig. 11. Urban Heat Island temporal dynamics, observed (30) and reconstructed

biofaçade numerically.

11. Model availability

A Python implementation of the proposed model is freely available at https://github.com/victorpozzobon/biofaçade.

Acknowledgements

Appendix - UHII(t) and UCII(t) reconstruction

Urban Heat Island temporal dynamic was reconstructed using the works of Montavez, Lai, and their coworkers (29, 30). Based on their observations, the UHII(t) dynamic was broken into three phases: 6 to 10 hours after sun dawn (taken as 10 hours based on Montavez observation in Europe), the UHII reaches its minimum (classically $UHII_{Basal}$ = + 0.5 K). Then, the UHII rises to its maximum in about 5 hours and stabilizes overnight. Mathematically, they are described as a downward cosine (Eq. 26), an upward cosine (up to the value given by Eq. 10, Eq. 27), and an overnight plateau (at the value given by Eq. 10, Eq. 28). For each day, the new value of UHII was evaluated. Then, the days were chained together. Figure 11 compares experimental observations (30) and numerical reconstruction (UHII of the previous day: 2.75 K, basal level: +0.5 K, UHII for the night to come: +2.5 K). As one can see, the agreement can be deemed satisfactory.

$$
\begin{aligned}
UHII(t) = {} & UHII_{Basal} \\
& + (UHII_{Previous\ day} - UHII_{Basal}) \\
& \frac{\cos(\pi \frac{t_{Solar} - t_{Sun\ dawn}}{10\ \text{hours}}) + 1}{2}
\end{aligned}
\tag{26}
$$

$$
\begin{aligned}
UHII(t) = {} & UHII_{Basal} \\
& + (UHII_{Current\ day} - UHII_{Basal}) \\
& \frac{-\cos(\pi \frac{t_{Solar} - t_{Sun\ dawn} - 10\ \text{hours}}{5\ \text{hours}}) + 1}{2}
\end{aligned}
\tag{27}
$$

$$
UHII(t) = UHII_{Current\ day}
\tag{28}
$$

In addition to the Urban Heat Island temporal dynamic, the Urban Cold Island temporal dynamic was also modeled. This phenomenon is the cold counterpart of the UHI. It happens transiently when the city mass is large enough to adsorb incident heat in such a large amount that the city center temperature is cooler than the closely rural area. This was identified in this work as when the UHII for a given day dropped below the basal level of +0.5 K. Mathematically, it is also described as three phases. First, a downward cosine (down to the negative value of the UHII, Eq. 29), an upward cosine (up to the basal value of +0.5 K, Eq. 30), and a plateau (at +0.5 K overnight (29), Eq. 31). With this model, Urban Heat and Cold Island phenomena can be described and chained indiscriminately.

$$
\begin{aligned}
UHII(t) = {} & UHII_{Current\ day} \\
& + (UHII_{Previous\ day} - UHII_{Current\ day}) \\
& \frac{\cos(\pi \frac{t_{Solar} - t_{Sun\ dawn}}{10\ \text{hours}}) + 1}{2}
\end{aligned}
\tag{29}
$$

$$UHII(t) = UHII_{Current\ day}$$
$$+ (UHII_{Basal} - UHII_{Current\ day})$$
$$\frac{-\cos(\pi \dfrac{t_{Solar} - t_{Sun\ dawn} - 10\ \text{hours}}{5\ \text{hours}}) + 1}{2}$$

$$\tag{30}$$

$$UHII(t) = UHII_{Basal} \tag{31}$$

Nomenclature

Latin symbols	Property	Unit
A	First parameter of Defraeye's correlation	-
B	Second parameter of Defraeye's correlation	$W/m^2/K$
CC	Cloud Cover factor	-
Cp	Specific heat	J/kg/K
E	Elevation above the ground	m
e	Thickness	m
F	View factor	-
f	Aeration	VVM (Vessel Volume per Minute)
H	Height	m
h	Convective heat transfer coefficient	$W/m^2/K$
I_0	Incident photosynthetically active light intensity	μPhotonPAR/m^2/s
$\overline{I}$	Volume-averaged photosynthetically active light intensity	μPhotonPAR/m^2/s
k	Thermal conductivity	W/m/K
L	Characteristic length	m
n_X	Number of X	-
P	Power	W
Pr	Prandtl number	-
Re	Reynolds number	-
R	Reflectivity	-
Ra	Rayleigh number	-
r	Surface roughness	m
T	Temperature	°C in the text / K in formulas
t	Time	s
U	Velocity	m/s
UHII	Urban Heat Island Intensity	K
w	Width	m
Y	Relative humidity	%

Greek symbols	Property	Unit
α	Green light transmitted fraction	-
ϵ	Emissivity	-
ζ	Refraction index	-
η	Efficiency	-
θ	Angle	rad
μ	Microalgae growth rate	1/day
ν	Kinematic viscosity	m²/s
ρ	Density	kg/m^3
σ	Boltzmann's constant	$W/m^2/K^4$
τ	Transmission	-
Φ	Heat flux	W/m^2

Subscript	Description
Abs	Absorbed by the culture
Air	Air, indoor or outdoor
Building	Building hosting the façade
Conv	Convective-conductive
Emi	Emitted
Forced	Forced convection
Free	Free convection
Gas	Sparged gas
Glaz	Glazing
i	Incidence
In	Indoor
Inlet	Gas injection
Interface	Interface
IR	Infrared
Max	Maximum
mc	Microalgae culture
Min	Minimum
Net	Net exchange
Opt	Optimal
Out	Outdoor
Outlet	Gas vent
pmma	PolyMethyl MethAcrylate
ps	Photosynthesis
r	Refraction
Rad	Radiative
Ref	Reference
Rur	Rural
Sky	Sky
Station	Meteorological station
Sun	Sun
Sur	Surrounding
Tot	Total
Urb	Urban
Vis	Visible
Water	Water
Wind	Wind

Bibliography

1. Maryam Talaei, Mohammadjavad Mahdavinejad, and Rahman Azari. Thermal and energy performance of algae bioreactive façades: A review. *Journal of Building Engineering*, 28: 101011, March 2020. ISSN 2352-7102. .

2. Rewaa Mahrous, Emanuela Giancola, Ahmed Osman, Takashi Asawa, and Hatem Mahmoud. Review of key factors that affect the implementation of bio-receptive façades in a hot arid climate: Case study north Egypt. *Building and Environment*, 214:108920, April 2022. ISSN 0360-1323. .

3. J. Pruvost, B. Le Gouic, O. Lepine, J. Legrand, and F. Le Borgne. Microalgae culture in building-integrated photobioreactors: Biomass production modelling and energetic analysis. *Chemical Engineering Journal*, 284:850–861, January 2016. ISSN 1385-8947. .

4. Emin Selahattin Umdu, Ilker Kahraman, Nurdan Yildirim, and Levent Bilir. Optimization of microalgae panel bioreactor thermal transmission property for building façade applications. *Energy and Buildings*, 175:113–120, September 2018. ISSN 0378-7788. .

5. Hanieh Sarmadi and Mohammadjavad Mahdavinejad. A designerly approach to Algae-

based large open office curtain wall Façades to integrated visual comfort and daylight efficiency. *Solar Energy*, 251:350–365, February 2023. ISSN 0038-092X. .

6. Ferial Ahmadi, Sara Wilkinson, Hamidreza Rezazadeh, Suraparb Keawsawasvong, Qodsiye Najafi, and Arash Masoumi. Energy efficient glazing: A comparison of microalgae photobioreactor and Iranian Orosi window designs. *Building and Environment*, 233:109942, April 2023. ISSN 0360-1323. .

7. Jan Wurm and Martin Pauli. SolarLeaf: The world's first bioreactive façade. *arq: Architectural Research Quarterly*, 20(1):73–79, March 2016. ISSN 1359-1355, 1474-0516. . Publisher: Cambridge University Press.

8. Ines Wagner, Christian Steinweg, and Clemens Posten. Mono- and dichromatic LED illumination leads to enhanced growth and energy conversion for high-efficiency cultivation of microalgae for application in space. *Biotechnology Journal*, 11(8):1060–1071, 2016. ISSN 1860-7314. . _eprint: https://onlinelibrary.wiley.com/doi/pdf/10.1002/biot.201500357.

9. Robert Dillschneider, Christian Steinweg, Rosa Rosello-Sastre, and Clemens Posten. Biofuels from microalgae: Photoconversion efficiency during lipid accumulation. *Bioresource Technology*, 142:647–654, August 2013. ISSN 0960-8524. .

10. Arthur Oliver, Cristobal Camarena-Bernard, Jules Lagirarde, and Victor Pozzobon. Assessment of Photosynthetic Carbon Capture versus Carbon Footprint of an Industrial Microalgal Process. *Applied Sciences*, 13(8):5193, January 2023. ISSN 2076-3417. . Number: 8 Publisher: Multidisciplinary Digital Publishing Institute.

11. Thomas D. Brock. Life at High Temperatures. *Science*, 230(4722):132–138, October 1985. ISSN 0036-8075, 1095-9203. .

12. Victor Pozzobon, Wendie Levasseur, Elise Viau, Emilie Michiels, Tiphaine Clément, and Patrick Perré. Machine learning processing of microalgae flow cytometry readings: illustrated with Chlorella vulgaris viability assays. *Journal of Applied Phycology*, 32(5):2967–2976, October 2020. ISSN 1573-5176. .

13. Recommended Practice for the Calculation of Daylight Availability. *Journal of the Illuminating Engineering Society*, 13(4):381–392, July 1984. ISSN null. . Publisher: Taylor & Francis _eprint: https://doi.org/10.1080/00994480.1984.10748791.

14. Joe A. Clarke. *Energy Simulation in Building Design*. Routledge, 2001. ISBN 978-0-7506-5082-3. Google-Books-ID: WH0VCiF8jkoC.

15. Se Woong Kim and Robert D. Brown. Urban heat island (UHI) intensity and magnitude estimations: A systematic literature review. *Science of The Total Environment*, 779:146389, July 2021. ISSN 0048-9697. .

16. Carl Safi, Bachar Zebib, Othmane Merah, Pierre-Yves Pontalier, and Carlos Vaca-Garcia. Morphology, composition, production, processing and applications of Chlorella vulgaris: A review. *Renewable and Sustainable Energy Reviews*, 35:265–278, July 2014. ISSN 1364-0321. .

17. Victor Pozzobon. Chlorella vulgaris cultivation under super high light intensity: An application of the flashing light effect. *Algal Research*, 68:102874, November 2022. ISSN 2211-9264. .

18. Wendie Levasseur, Patrick Perré, and Victor Pozzobon. Chlorella vulgaris acclimated cultivation under flashing light: An in-depth investigation under iso-actinic conditions. *Algal Research*, 70:102976, March 2023. ISSN 2211-9264. .

19. Aloice W. Mayo. Effects of temperature and pH on the kinetic growth of unialga Chlorella vulgaris cultures containing bacteria. *Water Environment Research*, 69(1):64–72, 1997. ISSN 1554-7531. . _eprint: https://onlinelibrary.wiley.com/doi/pdf/10.2175/106143097X125191.

20. Hamidreza Rezazadeh, Zahra Salahshoor, Ferial Ahmadi, and Farshad Nasrollahi. Reduction of carbon dioxide by bio-façades for sustainable development of the environment. *Environmental Engineering Research*, 27(2), 2022. ISBN: 1226-1025 Publisher: Korean Society of Environmental Engineers.

21. Razmig Kandilian, Antoine Soulies, Jeremy Pruvost, Benoit Rousseau, Jack Legrand, and Laurent Pilon. Simple method for measuring the spectral absorption cross-section of microalgae. *Chemical Engineering Science*, 146:357–368, June 2016. ISSN 0009-2509. .

22. Xin-Guang Zhu, Stephen P Long, and Donald R Ort. What is the maximum efficiency with which photosynthesis can convert solar energy into biomass? *Current Opinion in Biotechnology*, 19(2):153–159, April 2008. ISSN 0958-1669. .

23. John R. Howell, M. Pinar Mengüc, Kyle Daun, and Robert Siegel. *Thermal Radiation Heat Transfer*. CRC Press, Boca Raton, 7th edition edition, December 2020. ISBN 978-0-367-34707-9.

24. Rémi Waché, Tim Fielder, Will E. C. Dickinson, Joe L. Hall, Peter Adlington, Stephen J. Sweeney, and Steven K. Clowes. Selective light transmission as a leading innovation for solar swimming pool covers. *Solar Energy*, 207:388–397, September 2020. ISSN 0038-092X. .

25. Luca Evangelisti, Claudia Guattari, and Francesco Asdrubali. On the sky temperature models and their influence on buildings energy performance: A critical review. *Energy and Buildings*, 183:607–625, January 2019. ISSN 0378-7788. .

26. Tomáš Ficker. Letter to the editor: Revision of the universal sky temperature model. *Indoor and Built Environment*, 31(9):2366–2369, November 2022. ISSN 1420-326X. . Publisher: SAGE Publications Ltd STM.

27. F. P. Incropera and J. F. Thomas. A model for solar radiation conversion to algae in a shallow pond. *Solar Energy*, 20(2):157–165, January 1978. ISSN 0038-092X. .

28. Peter Hoffmann, Oliver Krueger, and K. Heinke Schlünzen. A statistical model for the urban heat island and its application to a climate change scenario. *International Journal of Climatology*, 32(8):1238–1248, 2012. ISSN 1097-0088. . _eprint: https://onlinelibrary.wiley.com/doi/pdf/10.1002/joc.2348.

29. Jiameng Lai, Wenfeng Zhan, Fan Huang, James Voogt, Benjamin Bechtel, Michael Allen, Shushi Peng, Falu Hong, Yongxue Liu, and Peijun Du. Identification of typical diurnal patterns for clear-sky climatology of surface urban heat islands. *Remote Sensing of Environment*, 217:203–220, November 2018. ISSN 0034-4257. .

30. Juan P. Montávez, Antonio Rodríguez, and Juan I. Jiménez. A study of the Urban Heat Island of Granada. *International Journal of Climatology*, 20(8):899–911, 2000. ISSN 1097-0088. . _eprint: https://onlinelibrary.wiley.com/doi/pdf/10.1002/1097-0088%2820000630%2920%3A8%3C899%3A%3AAID-JOC433%3E3.0.CO%3B2-I.

31. Kevin Gallo, Robert Hale, Dan Tarpley, and Yunyue Yu. Evaluation of the Relationship between Air and Land Surface Temperature under Clear- and Cloudy-Sky Conditions. *Journal of Applied Meteorology and Climatology*, 50(3):767–775, March 2011. ISSN 1558-8424, 1558-8432. . Publisher: American Meteorological Society Section: Journal of Applied Meteorology and Climatology.

32. Sheng Zhang, Dun Niu, and Zhang Lin. Mean radiant temperature calculated based on radiant heat dissipation of human body addressing effect of emissivity of inner surfaces of envelope. *Solar Energy*, 246:14–22, November 2022. ISSN 0038-092X. .

33. A. J. N. Khalifa and R. H. Marshall. Validation of heat transfer coefficients on interior building surfaces using a real-sized indoor test cell. *International Journal of Heat and Mass Transfer*, 33(10):2219–2236, October 1990. ISSN 0017-9310. .

34. Theodore L. Bergman, Adrienne S. Lavine, Frank P. Incropera, and David P. DeWitt. *Fundamentals of Heat and Mass Transfer, 8th Edition*. Wiley, 8th edition edition, May 2017.

35. Thijs Defraeye and Jan Carmeliet. A methodology to assess the influence of local wind conditions and building orientation on the convective heat transfer at building surfaces. *Environmental Modelling & Software*, 25(12):1813–1824, December 2010. ISSN 1364-8152. .

36. OSHA Technical Manual (OTM). Section III: Chapter 2: Recommendations for the Employer. Technical Report TED 01-00-015, Occupational Safety and Health Administration, 2023.

37. Quentin Béchet, Andy Shilton, and Benoit Guieysse. Modeling the effects of light and temperature on algae growth: State of the art and critical assessment for productivity prediction during outdoor cultivation. *Biotechnology Advances*, 31(8):1648–1663, 2013. ISSN 0734-9750. .

38. Olivier Bernard and Barbara Rémond. Validation of a simple model accounting for light and temperature effect on microalgal growth. *Bioresource Technology*, 123:520–527, November 2012. ISSN 0960-8524. .

39. Jörg Degen, Andrea Uebele, Axel Retze, Ulrike Schmid-Staiger, and Walter Trösch. A novel airlift photobioreactor with baffles for improved light utilization through the flashing light effect. *Journal of Biotechnology*, 92(2):89–94, December 2001. ISSN 0168-1656. .

40. M. J. Assael, S. Botsios, K. Gialou, and I. N. Metaxa. Thermal Conductivity of Polymethyl Methacrylate (PMMA) and Borosilicate Crown Glass BK7. *International Journal of Thermophysics*, 26(5):1595–1605, September 2005. ISSN 1572-9567. .

41. Philip E. Ciddor. Refractive index of air: new equations for the visible and near infrared. *Applied Optics*, 35(9):1566–1573, March 1996. ISSN 2155-3165. . Publisher: Optica Publishing Group.

42. George M. Hale and Marvin R. Querry. Optical Constants of Water in the 200-nm to 200-μm Wavelength Region. *Applied Optics*, 12(3):555–563, March 1973. ISSN 2155-3165. . Publisher: Optica Publishing Group.

43. Xiaoning Zhang, Jun Qiu, Xingcan Li, Junming Zhao, and Linhua Liu. Complex refractive indices measurements of polymers in visible and near-infrared bands. *Applied Optics*, 59(8):2337–2344, March 2020. ISSN 2155-3165. . Publisher: Optica Publishing Group.

44. Domien G. M. Beersma, Serge Daan, and Roelof A. Hut. Accuracy of Circadian Entrainment under Fluctuating Light Conditions: Contributions of Phase and Period Responses. *Journal of Biological Rhythms*, 14(4):320–329, August 1999. ISSN 0748-7304. . Publisher: SAGE Publications Inc.

45. Jason Quinn, Lenneke de Winter, and Thomas Bradley. Microalgae bulk growth model with application to industrial scale systems. *Bioresource Technology*, 102(8):5083–5092, April 2011. ISSN 0960-8524. .

46. Victor Pozzobon. Microalgae bio-reactive façade: Location and weather-based systematic optimization. *Building and Environment*, 253:111352, April 2024. ISSN 0360-1323. .

47. I. M Sobol. Global sensitivity indices for nonlinear mathematical models and their Monte Carlo estimates. *Mathematics and Computers in Simulation*, 55(1):271–280, February 2001. ISSN 0378-4754. .

48. Carla Balocco, Luca Mercatelli, Niccolò Azzali, Marco Meucci, and Giuseppe Grazzini. Experimental transmittance of polyethylene films in the solar and infrared wavelengths. *Solar Energy*, 165:199–205, May 2018. ISSN 0038-092X. .

49. Qiang Gao, Xiaomei Wu, and Dongming Wang. Effect of fluorine and niobium co-doping on boosting the NIR blocking performance of TiO2 nanoparticles for energy efficient window. *Solar Energy*, 238:60–68, May 2022. ISSN 0038-092X. .